DSC time-domain solution of Maxwell's equations

Zhenhai Shao [a], G.W. Wei [b,*], Shan Zhao [a]

[a] *Department of Computational Science, National University of Singapore, Singapore 117543, Singapore*
[b] *Department of Mathematics, Michigan State University, East Lansing, MI 48824, USA*

Abstract

A new computational algorithm, the discrete singular convolution (DSC), is introduced for solving scattering and guided wave problems described by time-domain Maxwell's equations. The DSC algorithm is utilized for the spatial discretization and the fourth-order Runge–Kutta scheme is used for the time advancing. Staggered meshes are used for electromagnetic fields. Four standard test problems, a hollow air-filled waveguide, a dielectric slab-loaded rectangular waveguide, a shield microstrip line and a dielectric square, are employed to illustrate the usefulness, to test the accuracy and to explore the limitation of the DSC algorithm. Results are compared with those of finite difference, scaling function multi-resolution time domain, and finite element-based high frequency structure simulator. Numerical experiments indicate that the present algorithm is a promising approach for achieving high accuracy in electromagnetic wave computations.
© 2003 Elsevier Science B.V. All rights reserved.

Keywords: Maxwell's equations; Time domain; Waveguide; Microstrip; Discrete singular convolution

1. Introduction

Computational electromagnetics (CEM), particularly, numerical simulation of the propagation and scattering of electromagnetic waves, has a wide variety of applications in science and engineering, including microwave circuits, optical devices, radar, telecommunication and antennas [1–19]. The success of CEM depends crucially on the availability of inexpensive, high-performance digital computers and the virtue of computational algorithms for the solution of Maxwell's equations. A variety of computational techniques have been used for CEM, including finite difference [1,2], finite volume [3], discontinuous Galerkin [4], wavelet analysis [5], Scaling function multi-resolution time domain method [6–8], integer lattice gas automata [9], hierarchical tangential vector finite elements [10], Nedelec tetrahedral element method [11], spectral methods [12] and other approaches [13–17]. Typically, grid methods used in CEM are either global, such as the fast Fourier transform, spectral methods and pseudospectral methods, or local, such as finite

---

* Corresponding author.
 E-mail address: wei@math.msu.edu (G.W. Wei).

difference, finite volume and finite element methods. Global methods are highly accurate but are cumbersome to implement in complex geometries and non-conventional boundary conditions. For example, a global method may converge slowly in a waveguide mode analysis due to irregular boundary conditions. In contrast, local methods are easy to implement for complex geometries and discontinuous boundary conditions. However, the accuracy of local methods is usually very low. There exists many problems in CEM which require both high computational accuracy and high numerical flexibility in handling complex geometries. These problems are characterized by a geometry which has a large domain size, i.e., the dimensions of the scatterer greatly exceed the wavelength of the incident wave. A typical example is the radar cross-section analysis of an entire airplane with an incident electromagnetic wave having a frequency of the order of 10 GHz. To deal with such problems, it is desirable to have a computational method that has both global methods' accuracy and local methods' flexibility.

Recently, the discrete singular convolution (DSC) algorithm was proposed as a potential approach for the computer realization of singular integrations [20–23]. The theory of distribution and wavelet analysis forms the mathematical foundation for the DSC. Sequences of approximations to the singular kernels of Hilbert type, Abel type and delta type were constructed. Applications are discussed to analytical signal processing, Radon transform and surface interpolation. Numerical solutions to differential equations are formulated via singular kernels of the delta type. By appropriately choosing the DSC kernels, the DSC approach exhibits global methods' accuracy for integration and local methods' flexibility in handling complex geometries and boundary conditions. The DSC algorithm found its success in solving the Navier–Stokes equations [24,25] and in structural analysis [23,26,27]. In particular, analyses of plates vibrating at extremely high frequency and with densely distributed internal supports [27] are very challenging tasks, for which conventional methods have encountered a great deal of numerical instability. The DSC algorithm found its success in resolving these problems. What is most relevant to the present study is the use of the DSC algorithm for electrostatic and waveguide model analyses, and for electromagnetic wave propagation in homogeneous media [28]. The objective of the present work is to further explore the utility of the DSC approach for solving Maxwell's equations with inhomogeneous media.

It is important to clarify the similarity and difference between the DSC algorithm and standard finite difference schemes, and the difference between the DSC and Fourier spectral method. First, the DSC algorithm is similar to high-order finite difference schemes in some aspects. But it is not simply another high-order finite difference. It differs from the standard finite difference scheme in the following aspects: (i) It can be much more accurate than a high-order finite difference scheme of the same stencils simply because there is a parameter in the DSC algorithm that can be adjusted to deliver higher accuracy. (ii) It is very easy for the DSC algorithm to generate as many as thousands of grid stencils for some special applications involving high frequency waves, which is still very difficult for the finite difference scheme because of the numerical instability in computing high-order Lagrange polynomials. The ability to handle high frequency (short) waves is the central issue for all high-order methods. However, at present, most existing high-order methods cannot really handle hundreds of wavelengths required for the practical computation of the radar cross-section of a large airplane. We believe that the present method has potential for such an application. (iii) Unlike the Lagrange kernel or the high-order finite difference, which becomes the Fourier spectral method at the limit of infinitely many grid points and global support [29], the DSC algorithm does not converge to the Fourier spectral method under the same limit because the former has a Gaussian factor. Secondly, it is true that the DSC algorithm can be as accurate as the classical Fourier spectral method and a detailed numerical comparison and justification of this point was given [30]. But the DSC algorithm differs dramatically from the Fourier spectral method because of the follows: (i) The treatment of boundary conditions is different in two methods. Fourier spectral method requires the periodic boundary or the assistance of other techniques, such as perfectly matched layer (PML) [31]. In contrast, the DSC algorithm can directly handle a variety of different boundary conditions, such as periodic, Dirichlet, Neumann and Robin [20]. In fact, DSC algorithm has been successfully implemented in much more complicated cases

required by structural analysis involving (fourth-order) biharmonic equations, where boundary conditions are given by second-order partial differential equations [23]. (ii) The DSC algorithm can be directly implemented in eigenvalue problems in structural analysis where complex internal supports are presented [27]. Obviously, Fourier spectral method cannot be directly applied in this kind of problems. Problems of similar difficulties occur in the eigenvalue problem of optical waveguides, which involves dielectric inhomogeneity. For these reasons, the DSC algorithm is a new promising approach for the computational electromagnetic and solution of Maxwell's equations.

This paper is organized as follows. The DSC algorithm is briefly reviewed in Section 2. In Section 3, a discrete singular convolution time domain (DSCTD) treatment of Maxwell's equations is presented and four test examples are utilized to illustrate the usefulness, test the accuracy and explore the limitation of the DSC algorithm. This paper ends with a conclusion.

2. The Discrete singular convolution

Singular convolutions are a special class of mathematical transformations, which appear in many science and engineering problems. It is most convenient to discuss singular convolutions in the context of the theory of distributions. The latter has a significant impact in mathematical analysis. It provides a rigorous justification for a number of informal manipulations in engineering and has significant influence over many mathematical disciplines, such as operator calculus, differential equations, functional analysis, harmonic analysis, harmonic analysis and transformation theory. Let T be distribution and $\eta(t)$ be an element of the space of test functions. A singular convolution is defined as

$$F(t) = (T * \eta)(t) = \int_{-\infty}^{\infty} T(t-x)\eta(x)\,dx. \tag{1}$$

Here $T(t-x)$ is a singular kernel. Depending on the form of the kernel T, the singular convolution is the central issue for a wide range of science and engineering problems, such as Hilbert transform, Abel transform and Radon transform. In the present study, only Singular kernels of the delta type are required

$$T(x) = \delta^{(n)}(x) \quad (n = 0, 1, 2, \ldots). \tag{2}$$

Here, kernel $T(x) = \delta(x)$ is of particular importance for interpolation of surfaces and curves. Higher-order kernels, $T(x) = \delta^{(n)}$ $(n = 1, 2, \ldots)$ are essential for numerically solving partial differential equations and for image processing, noise estimation, etc. However since these kernels are singular, they cannot be directly digitized in computers. Hence, the singular convolution (1), is of little numerical merit. To avoid the difficulty of using singular expressions directly in computer, we construct sequences of approximations (T_α) to the distribution T

$$\lim_{\alpha \to \alpha_0} T_\alpha(x) \to T(x), \tag{3}$$

where α_0 is a generalized limit. Obviously, in the case of $T(x) = \delta(x)$, each element in the sequence, $T_\alpha(x)$, is a delta sequence kernel. With a sufficiently smooth approximation, it is useful to consider a discrete singular convolution (DSC)

$$F_\alpha(t) = \sum_k T_\alpha(t - x_k)f(x_k), \tag{4}$$

where $F_\alpha(t)$ is an approximation to $F(t)$ and $\{x_k\}$ is an appropriate set of discrete points on which the DSC (4) is well defined. Note that, the original test function $\eta(x)$ has been replaced by $f(x)$.

A typical example is Shannon's delta kernel, which is given by the following (inverse) Fourier transform of the characteristic function, $\chi[-\alpha, \alpha]$,

$$\delta_\alpha(x) = \frac{1}{2\pi} \int_{-\infty}^{\infty} \chi_{[-\alpha,\alpha]} e^{i\xi x} \, d\xi = \frac{\sin(\alpha x)}{\pi x}. \tag{5}$$

For the purpose of digital computation, it is necessary to discretize delta kernels. To this end, we should examine a sampling basis given by Shannon's delta kernel

$$S_k(x) = \frac{\sin \pi(x - x_k)}{\pi(x - x_k)}. \tag{6}$$

This sampling basis is also an element of the Paley–Wiener reproducing kernel Hilbert space. It provides a discrete representation of every (continuous) function in B_π^2, that is

$$f(x) = \sum_{k \in Z} f(x_k) S_k(x) \quad \forall k \in B_\pi^2. \tag{7}$$

This is Shannon's sampling theorem and it means that one can recover a continuous bandlimited L^2 function from a set of discrete values. Shannon's delta kernel is obviously interpolative

$$S_n(x_m) = \delta_{n,m}, \tag{8}$$

where $\delta_{n,m}$ is the Kronecker delta function. Computationally, being interpolative is desirable for numerical accuracy and simplicity.

Eq. (7) can never be realized because it requires infinitely many sampling points. A truncation is required in practical computations. Unfortunately, Shannon's delta kernel decays slowly and leads to substantial errors. According to the theory of distributions, the smoothness, regularity and localization of a temper distribution can be improved by regularization with a function of the Schwartz class. We apply this principle to regularize singular convolution kernels [32]

$$\delta_{\sigma,\alpha}(x) = R_\sigma(x) \delta_\alpha(x) \quad (\sigma > 0), \tag{9}$$

where R_σ is a Gaussian regularizer $R_\sigma(x) = \exp[-x^2/2\sigma^2]$. The parameter σ determines the width of the Gaussian envelop and is commonly varied in association with the grid spacing Δ, i.e., $\sigma = r\Delta$. One needs to set the value of r before computation. Note that r is independent of the spacing Δ. The Gaussian regularizer is a Schwartz class function and has excellent numerical performance. Many other regularizers was discussed by Gottlieb and Shu [33]. The truncation error is dramatically reduced by the use of a delta regularizer. The regularized Shannon's delta kernel (RSK) on an arbitrary grid is given by

$$\delta_{\sigma,\Delta}(x - x_k) = \frac{\sin(\pi/\Delta)(x - x_k)}{(\pi/\Delta)(x - x_k)} \exp\left\{ -\frac{(x - x_k)^2}{2\sigma^2} \right\}. \tag{10}$$

In this manner, a function and its nth-order derivative are approximated in the present algorithm as

$$f^{(n)}(x) \approx \sum_{k=-M}^{M} \delta_{\sigma,\Delta}^{(n)}(x - x_k) f(x_k) \quad (n = 0, 1, 2, \ldots), \tag{11}$$

where $\delta_{\sigma,\Delta}(x - x_k)$ is a collective symbol for any (regularized) delta kernel, and $2M + 1$ is the computational bandwidth. The higher-order derivative terms $\delta_{\sigma,\Delta}^{(n)}(x - x_k)$ are given by

$$\delta_{\sigma,\Delta}^{(n)}(x - x_k) = \left(\frac{d}{dx}\right)^n \delta_{\sigma,\Delta}(x - x_k). \tag{12}$$

Here, the differentiation can be carried out analytically. Numerical solution of differential equations can be easily implemented in collocation by using Eq. (11).

In order to examine the numerical resolution of the DSC algorithm, and to optimally choose the DSC parameters, i.e., the computational bandwidth M and the scaled Gaussian window size r, we conduct a discrete Fourier analysis. Fourier analysis is a classical technique for characterizing the Fourier resolution of an interpolation or differentiation scheme applied to a class of compactly supported and periodic functions [34]. Thus, the Fourier analysis is capable to provide an effective way to quantify the accuracy of approximation schemes.

Because the derivatives are approximated by means of discrete convolution [Eq. (11)] in the DSC algorithm, the corresponding Fourier coefficients of spatial derivatives can be expressed as

$$\mathscr{F}[f^{(n)}(x)] = \mathscr{F}\left[\delta_{\sigma,\Delta}^{(n)}(x)\right] \times \mathscr{F}[f(x)], \tag{13}$$

where $\mathscr{F}$ denotes the Fourier transform

$$\mathscr{F}[f(x)] = \frac{1}{2\pi} \int_{-\infty}^{\infty} f(x)\, e^{ikx}\, dx. \tag{14}$$

We will only consider the first derivative approximation which is used in the numerical solution of time-domain Maxwell's equations. Analytically, we have

$$\mathscr{F}\left[\frac{\partial f}{\partial x}\right] = ik\mathscr{F}[f(x)]. \tag{15}$$

For simplicity, we denote $k^* = -i\mathscr{F}[\delta_{\sigma,\Delta}^{(n)}(x)]$ and introduce the scaled wavenumbers $\omega^* = \Delta k^*$ and $\omega = \Delta k$, and a scaled coordinate $s = x/\Delta$. Then, the approximation error of the DSC algorithm can be measured by the closeness of ω^* to ω within the domain of the wavenumber $\omega \in [-\pi, \pi]$. Note that since the DSC approximation to the first-order derivative operator is anti-symmetric, it produces no amplitude error, i.e., it admits no error in the real part of its Fourier response.

The dispersive errors of the central finite difference (FD) and DSC schemes are illustrated in Fig. 1, where the discrete Fourier transform is used to calculate ω^*. It can be observed that the DSC scheme can
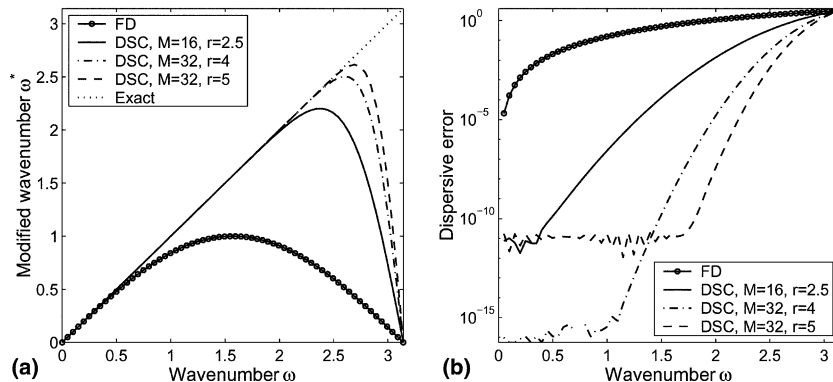

Fig. 1. Plot of dispersion errors. (a) The modified wavenumbers vs wavenumber; (b) the difference between the modified wavenumber ω^* and wavenumber ω in the log scale.

stay very close to the exact differentiation except for very high wavenumbers, while the FD scheme deviates from the exact derivative very quickly.

Modified wavenumbers associated with several DSC parameters are also depicted in Fig. 1. These plots actually provide an intuitive means for comparing different DSC kernels and for optimizing DSC parameters. It is clear that when M is larger, the dispersive error becomes smaller. This agrees with the previous finding that the DSC algorithm can provide controllable accuracy by varying the parameter M [21]. Furthermore, it can be seen from Fig. 1 that for a fixed M, the dispersive errors of the DSC kernels can be controlled by adjusting $r = \sigma/\Delta$. It appears from Fig. 1(a) that the modified wavenumber ω^* gives a better approximation to the wavenumber ω, especially in the high wavenumber region, when a large r value is used. However, as indicated in Fig. 1(b), when r is too large, the dispersive error for low wavenumbers become quite large. Therefore, the ratio r governs the trade-off between the accuracy for the low frequency part and that for the high frequency part in the DSC algorithm. In summary, by means of the Fourier analysis, one can select the desired DSC parameters M and r according to the nature of the problem under consideration. For more details, we refer to [35].

3. Applications

In this work, we develop a DSCTD approach for time domain wave computations. Physically, a guided wave structure is either an open type or a closed type and is generally three-dimensional. Maxwell's equations are the starting point for such computations. In their differential form, these equations are

$$\frac{\partial \mathbf{B}}{\partial t} = -\nabla \times \mathbf{E}, \tag{16}$$

$$\frac{\partial \mathbf{D}}{\partial t} = \nabla \times \mathbf{H}, \tag{17}$$

where $\mathbf{E}$ is the electric field, $\mathbf{D}$ electric flux density and $\mathbf{D} = \epsilon \mathbf{E}$; $\mathbf{H}$ is the magnetic field, $\mathbf{B}$ is the magnetic flux density and $\mathbf{B} = \mu \mathbf{H}$. Usually, a waveguide has a uniform cross-section in its longitudinal direction along which the electromagnetic signal power is transmitted. As such, the electric and magnetic field variations φ along the z-coordinate axis of the closed waveguide geometries can be written as

$$\varphi(x, y, z) = \varphi(x, y) \, e^{-j\beta z}, \tag{18}$$

where β is the axial propagation constant. Consequently, Maxwell's equations reduce to their two dimensional (2D) form [18,19].

In the present investigation, we focus on 2D waveguide problems [18]. A staggered grid system as shown in Fig. 2 is employed, which is essentially an extension of the standard Yee cell. We use the DSC algorithm to approximate the spatial derivative of Maxwell's equations as follows:

$$f^{(n)}(x) \approx \sum_{k=-M}^{-1} \delta_{\sigma,\Delta}^{(n)}\left(x - x_{k+\frac{1}{2}}\right) f\left(x_{k+\frac{1}{2}}\right) + \sum_{k=1}^{M} \delta_{\sigma,\Delta}^{(n)}\left(x - x_{k-\frac{1}{2}}\right) f\left(x_{k-\frac{1}{2}}\right), \tag{19}$$

where $x_{k+1/2}$ and $x_{k-1/2}$ are centered around x, n is the order of derivative, $\delta_{\sigma,\Delta}$ is a collective symbol for any (regularized) DSC kernels [20,23]. In the following examples, unless specified, the RSK is used for the spatial discretization and the fourth-order explicit Runge–Kutta (RK4) scheme is used for the time discretization.
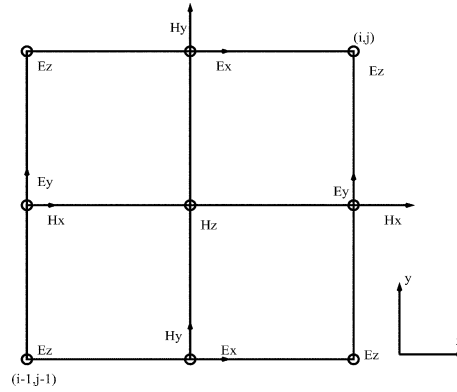
Fig. 2. Staggered grid system.

The final discrete equation for H_z in $n+1$ time steps and mesh point (i,j) is shown as follows:

$$
\begin{aligned}
H_z^{(n+l)}(i,j) = H_z^{(n)}(i,j) + \frac{\tilde{l}}{\mu} \Bigg\{ & \Bigg[\sum_{s=-M_y}^{-1} \delta_{\sigma,\Delta_y}^{(1)}\left(\left(s+\frac{1}{2}\right)\Delta_y\right) E_x^{(n+l-1/4)}\left(i,j+s+\frac{1}{2}\right) \\
& + \sum_{s=1}^{M_y} \delta_{\sigma,\Delta_y}^{(1)}\left(\left(s-\frac{1}{2}\right)\Delta_y\right) E_x^{(n+l-1/4)}\left(i,j+s-\frac{1}{2}\right) \Bigg] \\
& - \Bigg[\sum_{s=-M_x}^{-1} \delta_{\sigma,\Delta_x}^{(1)}\left(\left(s+\frac{1}{2}\right)\Delta_x\right) E_y^{(n+l-1/4)}\left(i+s+\frac{1}{2},j\right) \\
& + \sum_{s=1}^{M_x} \delta_{\sigma,\Delta_x}^{(1)}\left(\left(s-\frac{1}{2}\right)\Delta_x\right) E_y^{(n+l-1/4)}\left(i+s-\frac{1}{2},j\right) \Bigg] \Bigg\},
\end{aligned}
$$

(20)

where M_x, M_y are bandwidth in x- and y-directions, respectively. Here l is Runge–Kutta steps and chosen as 1/4, 2/4 and 3/4. Correspondingly, the Runge–Kutta coefficient $\tilde{l}$ is set to $\tilde{l} = 1/2$, 1/2, and 1 for $l = 1/4$, 2/4 and 3/4, respectively.

As the DSC kernels are either symmetric or antisymmetric, they would require approximating the function values outside the computational domain. For perfect electric wall, tangential electric fields E_t and normal magnetic field H_n outside the computational domain are obtained by anti-symmetric extensions [20], whereas, for normal electric field E_n and tangential magnetic fields H_t, symmetric extensions are used. For perfect magnetic wall, tangential magnetic fields H_t and normal electric field E_n outside the computational domain are obtained by anti-symmetric extensions [20], whereas, for normal magnetic field H_n and tangential electric fields E_t, symmetric extensions are used. For periodic boundary, all electric and magnetic fields outside the computational domain are obtained from the values within the domain.

3.1. Hollow rectangular waveguide

To illustrate the potential of the DSC algorithm for electromagnetic wave simulations, we first consider the air-filled rectangular waveguide [18]. The cross-section of such a hollow rectangular close-type waveguide is shown in Fig. 3. This is one of the simplest problems in waveguide analyses and it is analytically solvable. The initial value of the problem is given by:
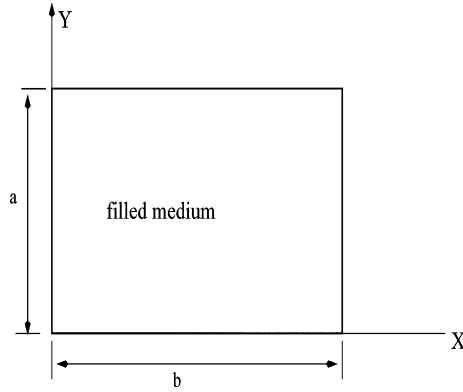
Fig. 3. Filled waveguide.

$$E_{zr}(x, y, 0) = \sin\left(\frac{m\pi}{a}x\right)\sin\left(\frac{n\pi}{b}y\right),$$

$$E_{xi}(x, y, 0) = -\frac{\beta}{h^2}\cos\left(\frac{m\pi}{a}x\right)\sin\left(\frac{n\pi}{b}y\right),$$

$$E_{yi}(x, y, 0) = -\frac{\beta}{h^2}\sin\left(\frac{m\pi}{a}x\right)\cos\left(\frac{n\pi}{b}y\right),$$

(21)

where a, b are the lengths in the x- and y-directions, respectively,

$$h = \sqrt{\left(\frac{m\pi}{a}\right)^2 + \left(\frac{n\pi}{b}\right)^2}$$

(22)

and

$$\beta = \sqrt{k^2 - h^2} = \sqrt{w^2\mu\epsilon - \left(\frac{m\pi}{a}\right)^2 - \left(\frac{n\pi}{b}\right)^2}.$$

(23)

Here the subscripts r and i refer to the real and imaginary components, respectively. The frequency f can be obtained from Eq. (23)

$$f = \frac{1}{2\pi\sqrt{\mu\epsilon}}\sqrt{\beta^2 + \left(\frac{m\pi}{a}\right)^2 + \left(\frac{n\pi}{b}\right)^2}.$$

(24)

For this set of initial values, the analytical solution of $E_{zr}(x, y, t)$ can be given by

$$E_{zr}(x, y, t) = \sin\left(\frac{m\pi}{a}x\right)\sin\left(\frac{n\pi}{b}y\right)\cos(wt).$$

(25)

In the present computations, the geometric lengths along the x- and y-directions are taken as $a = b = 10\pi$ m and are both discretized by using N grid points. A small time increments $\Delta t = 0.001$ are used so that the major source of errors is due to the spatial discretization. The dominant mode TM_{11} is considered with a variety of mesh size N and computational bandwidth M. The L_∞ errors are computed as

$$L_\infty = \max_{\forall x_i, y_j \in \Omega} |E_{zr}(x_i, y_j, t) - \bar{E}_{zr}(x_i, y_j, t)|,$$

where $\bar{E}_{zr}$ is the numerical result and Ω is the computational domain. Both the second-order time discretization and the RK4 schemes are used for the time advancing. Table 1 lists the L_∞ errors from the

Table 1
L_∞ errors for solving the TM11 mode of a waveguide ($\Delta t = 0.001$)

Time	Second-order time scheme			Fourth-order Runge–Kutta			
	FDTD	S-MRTD	DSCTD	S-MRTD		DSCTD	
	$N = 24$	$N = 24$, $M = 9$	$N = 24$, $M = 9$, $r = 1.9$	$N = 24$, $M = 9$	$N = 24$, $M = 9$, $r = 1.9$	$N = M = 24$, $r = 2.9$	$N = M = 12$, $r = 2.1$
2	3.97(−3)	6.57(−3)	3.95(−3)	6.17(−3)	4.83(−6)	1.43(−14)	2.40(−08)
6	1.55(−2)	1.18(−2)	3.95(−3)	1.12(−2)	9.19(−6)	3.22(−14)	4.57(−08)
10	1.55(−2)	1.18(−2)	3.96(−3)	1.12(−2)	9.19(−6)	3.33(−14)	4.57(−08)
14	1.55(−2)	1.21(−2)	3.96(−3)	1.12(−2)	9.19(−6)	4.77(−14)	4.66(−08)
18	1.55(−2)	1.21(−2)	3.97(−3)	1.12(−2)	9.38(−6)	6.05(−14)	4.66(−08)
22	1.55(−2)	1.26(−2)	3.98(−3)	1.12(−2)	9.73(−6)	8.50(−14)	4.84(−08)
CPU	27	109	104	388	392	832	126

FDTD [1], S-MRTD [6] and DSCTD approximations. The Battle–Lemarie scaling function [6] is used for the S-MRTD method. It can be seen that, by using the second-order time scheme, the S-MRTD is slightly more accurate than the FDTD, while the DSCTD algorithm is considerably more accurate than both FDTD and S-MRTD. However, its accuracy is still limited by errors in the time discretization. When the RK4 is used, the DSCTD scheme improves nearly 1000 times in accuracy, whereas, the accuracy of the S-MRTD is essentially unchanged. The present DSCTD scheme is of machine precision when $M = 24$.

As both the S-MRTD and DSCTD have large computational bandwidths, they cost more computational time than the FDTD scheme. To fairly assess these schemes, the CPU time used for each computation is also listed in Table 1. By using the second-order time scheme, the DSCTD requires four times CPU as much as the FDTD and is overall more efficient because it is at least four times more accurate. When the RK4 is used, the DSCTD ($N = M = 24$) costs 16 times more CPU but is about 10^{11} times more accurate than the FDTD scheme. When the parameter $M = 9$ is used, both S-MRTD and DSCTD methods have the same computational bandwidth and cost a similar amount of CPU time. Obviously, the DSC approach is much more efficient in this case. However, we note that since the S-MRTD method is a general approach [6–8], it is possible to improve its results by using a better scaling function.

It has been shown in the Fourier analysis that the DSC algorithm can provide controllable accuracy by varying the parameter M. It is interesting to numerically verify this. To this end, we first consider a number of computations with different mesh size N. Four values are tested $N = 3$, 6, 12 and 24, and we choose $M = N$ with r being optimally selected. For the TM11 mode and $\Delta t = 0.001$, the L_∞ errors of the DSCTD are found to be 5.384×10^{-2}, 5.72×10^{-4}, 2.4×10^{-8} and 1.43×10^{-14}, respectively, for $N = 3$, 6, 12 and 24. Thus, the increments in accuracy when doubling M (and N) for this problem are $2^{6.6}$, $2^{14.5}$ and $2^{20.7}$, respectively. Such increments are clearly of exponential rate. The machine accuracy is reached when $M = 24$.

We next examine the error as a function of the bandwidth parameter M for a fixed grid $N = 36$, see Fig. 4. Here the wavelength is fixed as $\lambda = c/f = 8$ and the time increment is still $\Delta t = 0.001$. The ratio r is optimally chosen for each M. It is seen from Fig. 4 that, similar, the approximation errors decay exponentially as M increases, until M is larger than 20, where the accuracy is limited by the machine precision. Thus, based on both experiments, one can conclude that the DSCTD algorithm is able to achieve the spectral accuracy of global methods. This finding is in consistent with the previous theoretical study [35]. Furthermore, it is noted that by using different M, the DSCTD can provide different level of accuracy. Therefore, one of the advantages of the DSCTD algorithm is its robustness, and allows the selection of desirable accuracy for a given problem without any need to change one's computer code.
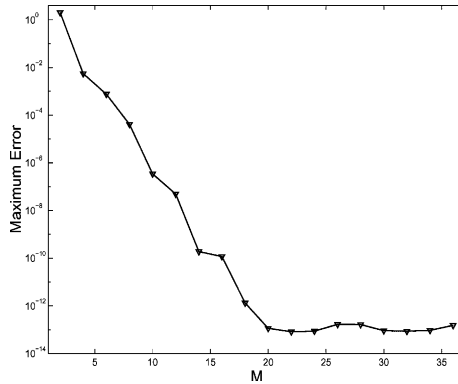
Fig. 4. L_∞ errors of RSK results with different bandwidths.

Due to its spectral accuracy [35], another advantage of the DSCTD algorithm is its capability to accurately approximate the propagation of high frequency waves. To see this, we further test the numerical accuracy of the proposed method against wavelength $\lambda = c/f$. The standard FDTD [1] is employed for a comparison. We choose $N = 36$ and $\Delta t = 0.0005$ for both the DSCTD and FDTD computations. For the DSCTD, we select $M = 32$ and $r = 3.5$. The computational results are plotted in Fig. 5. It is clear that as wavelength λ is very small, i.e., very high frequency waves are modeled, the accuracy of the FDTD is very low. However, for such a difficult case, the DSC results are significantly better than those of the FDTD and their errors are less than 10^{-6}. When λ is large (low frequency waves), the DSCTD algorithm can even outperform the FDTD by a factor of 10^{-12} in L_∞ errors. As a consequence, to achieve the same level of accuracy, the DSCTD requires much less grid points than those of the FDTD. Therefore, the DSCTD algorithm is cost-efficient.

Another interesting problem concerning the hollow air-filled waveguide is the numerical prediction of mode cutoff frequency [18]. To numerically calculate mode cutoff frequency in time domain, one should simulate the temporal variation of an initial excitation field inside the waveguide. For efficiency, the initial assigned field should be such that it is capable of exciting every possible TM (or TE) mode in the cavity-type close rectangular geometry. One good example suggested in [18] is a Gaussian pulse. To estimate TM mode cutoff frequencies, we can simply choose the axial electric field as [18]
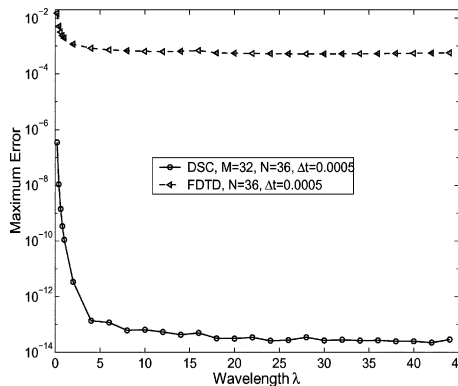

Fig. 5. L_∞ errors of the DSC and FDTD results vs wavelength.

$$E_{zr}(t=0) = A \exp\left\{ -\frac{(x-x_c)^2 + (y-y_c)^2}{2\tau^2} \right\}, \tag{26}$$

for $x \geqslant x_c$ and $y \geqslant y_c$, where (x_c, y_c) is the central node. In other words, only a quarter of the distribution of Gaussian pulse is used. The other electromagnetic fields are assumed to be zero.

In the present study, by setting $A = 100$ and $\tau = 0.0018$, the wave propagation of TM polarization is simulated by both the DSCTD and FDTD. The lengths of the waveguide along the x- and y-coordinates are 0.01 and 0.02, respectively. The spatial meshes $N_x = 51$, $N_y = 101$, and the bandwidth parameters $M_x = M_y = M = 24$ are chosen. For determining the mode cutoff frequencies, we record the temporal variation of E_z at a single spatial cell within the waveguide, e.g., $i = 5$ and $j = 5$. Then the discrete Fourier transform will be employed to transform the generated time series to its Fourier representation. The resulted spectrum will show isolated spike-like peaks which are in fact the mode cutoff frequencies of the hollow rectangular waveguide. The fast Fourier transform (FFT) may be used to speed up numerical computation.

The cutoff frequencies estimated by DSCTD and FDTD are shown in Table 2. Here the time domain computation is advanced until the time $t = N_t\Delta t = 8$, where N_t is the total time steps. The analytical mode cutoff frequencies are available [18] and can be exactly obtained from Eq. (24) by choosing $\beta = 0$. The analytical values are also tabulated in Table 2.

It should be emphasized that since estimated mode cutoff frequencies are locations of peaks, their values are just the coordinates of the spectrum. Note that the coordinate of the spectrum, f, is a set of discrete values in numerical computation. Therefore, the accuracy of estimated cutoff frequency is inevitably confined by the spectral spacing Δf, which is given as

$$\Delta f = \frac{c_0}{t} = \frac{c_0}{N_t\Delta t}, \tag{27}$$

Table 2
Mode cutoff frequencies (GHz) of hollow rectangular waveguide, TM polarization

m,n	f_c	RSK		FDTD		m,n	f_c	RSK		FDTD	
		$\hat{f}_c$	e_f	$\hat{f}_c$	e_f			$\hat{f}_c$	e_f	$\hat{f}_c$	e_f
1,1	16.7705	16.7625	0	16.7625	0	5,5	83.8525	83.8501	0	83.5502	8
1,4	33.5410	33.5250	0	33.5250	0	5,7	91.5492	91.5376	0	90.7127	4
1,5	40.3887	40.3876	0	40.3501	1	5,8	96.0469	96.0377	0	94.3502	45
1,8	61.8466	61.8376	0	61.6876	4	6,1	90.3119	90.3001	0	89.7752	14
2,1	30.9233	30.9375	0	30.9000	1	6,4	94.8683	94.8751	0	93.6002	34
2,2	33.5410	33.5250	0	33.5250	0	6,7	104.1933	104.2127	1	103.6877	13
2,6	54.0833	54.0751	0	54.0001	2	6,9	112.5000	112.5002	0	111.0002	40
2,9	73.8664	73.8751	0	73.6501	6	7,1	105.2675	105.2627	0	104.4377	22
3,1	45.6207	45.6376	0	45.5626	2	7,5	111.4955	111.4877	0	110.7002	21
3,3	50.3115	50.3251	0	50.2501	2	7,7	117.3936	117.4126	1	116.5503	22
3,7	69.1466	69.1501	0	69.0376	3	7,9	124.8249	124.8378	0	124.0128	22
3,9	81.1249	81.1127	0	80.8877	6	8,1	120.2341	120.2253	0	118.9878	33
4,1	60.4669	60.4501	0	60.3751	2	8,4	123.6932	123.6753	0	122.2878	37
4,4	67.0820	67.0501	1	67.1253	1	8,8	134.1641	134.1753	0	132.9753	32
4,6	75.0000	75.0002	0	74.8501	4	8,9	137.6817	137.6628	1	136.5753	30
4,9	90.3119	90.3002	0	89.7752	14	9,1	135.2082	135.2253	0	134.1753	28
5,1	75.3740	75.3752	0	74.8501	14	9,4	138.2932	138.3003	0	137.3253	26
5,3	78.3023	78.3002	0	78.0001	8	9,7	144.8491	144.8628	0	143.1753	45
5,4	80.7775	80.7752	0	80.4752	8	9,9	150.9346	150.9378	0	149.2503	45

Here $t = 8$, thus $\Delta f = 0.0375$ GHz.

where c_0 is the speed of light in free space and is chosen as 3.0×10^8 m/s. Consequently, for a particular mode cutoff frequency f_c and a fixed Δf, an estimate within the range $[f_c - (\Delta f/2), f_c + (\Delta f/2)]$ can actually be regarded as *exact* in terms of the used Δf. This is because, no matter how accurate the method is used in time domain for wave simulation, the estimated mode cutoff frequency $\hat{f}_c$ can at most be randomly distributed in the interval $[f_c - (\Delta f/2), f_c + (\Delta f/2)]$. If a more accurate estimate is expected, a smaller Δf has to be used. However, since the time increment Δt is limited by the CFL stability condition, this can only be achieved by using a larger N_t, which implies more expensive computations.

To achieve an in-depth understanding of our computational results, we define the following error measurement:

$$e_f = \left\lfloor \frac{|f_c - \hat{f}_c|}{\Delta f} \right\rceil, \tag{28}$$

where $\lfloor x \rceil$ denotes rounding x to the nearest integer. Obvious, $e_f = 0$ means that the exact estimate is obtained in sense of the present Δf. In general, the value e_f measures the deviation of $\hat{f}_c$, in terms of Δf, from the true mode cutoff frequency f_c. The frequency errors of DSCTD and FDTD estimates are calculated and listed in Table 2. It can be observed that, at very low frequency (below 35 GHz), the results obtained by using the FDTD method have an acceptable accuracy. With the increase of frequency, the frequency errors of the FDTD estimates increase significantly. When the frequency exceeds 90.00 GHz, the FDTD results become unreliable since they usually differ from the analytical values by dozens of Δf. For mode $(9,9)$, the error of the FDTD is as large as $45\Delta f$. On the contrary, the DSCTD estimates are very accurate up to mode $(9,9)$ or 150 GHz. Most of DSCTD estimates in Table 2 are exact in terms of the Δf. Only a few ones have a very small error with single Δf deviation. Therefore, the DSCTD estimation of mode cutoff frequency of hollow rectangular waveguide is extremely accurate.

3.2. Dielectric slab-loaded rectangular waveguide

Numerical simulation of a rectangular waveguide which is partially loaded with a slab of dielectric material [18] is discussed in this section. This problem is selected to test the DSCTD algorithm for treating inhomogeneous media. The dielectric slab is located vertically on the right side of rectangular waveguide as shown in Fig. 6. The relative permittivity and permeability of the dielectric slab are $\epsilon_r = 11.7$ and $\mu_r = 1$, respectively. The lengths for the rectangular waveguide along the x- and y-coordinates are $a = 0.02$ and $b = 0.01$ m, and the unfilled empty rectangular region has the width of $d = 0.01$ m. The same initial impulse excitation as in the former example, Eq. (26), is used to initiate field E_z.

To validate the results of cutoff frequencies, analytical expressions are utilized. The analytical expression for the cutoff frequencies for two types of normal modes can be found in [18]. For LSE mode and LSM mode, cutoff frequencies are given by

$$f_c = \frac{c_0}{2\pi} \left[h^2 + \left(\frac{m\pi}{b} \right)^2 \right]^2. \tag{29}$$

For LSE modes, the parameters p and h are obtained from the following of transcendental equations:

$$h \tan[p(a - d)] = -p \tan(hd), \tag{30}$$

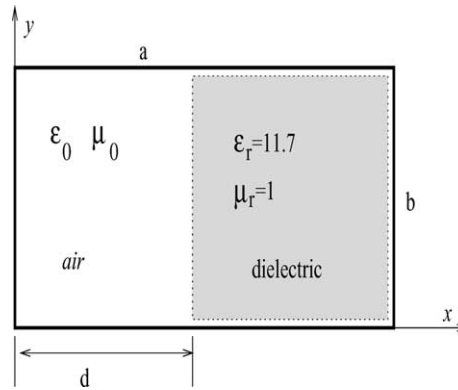$$p^2 = h^2 + (\epsilon_r - 1)k^2. \tag{31}$$

Fig. 6. Partially filled rectangular waveguide.

For LSM modes, the parameters p and h are of the form

$$-p\tan[p(a-d)] = h\epsilon_r \tan(hd), \tag{32}$$

$$p^2 = h^2 + (\epsilon_r - 1)k^2, \tag{33}$$

where $k^2 = w^2\epsilon_0\mu_0$.

For the z-polarization of TM modes, the interior region of the rectangular cross-section is modeled by discretizing the region into structured square cells, $\Delta x = \Delta y = \Delta$. Computational bandwidth is $M_x = M_y$ along x- and y-directions, respectively. The mode cutoff frequencies are estimated similarly by means of Fourier transform. Two sets of numerical discretization parameters are considered, see Table 3. For cutoff frequency estimates of the DSCTD and FDTD, the frequency errors defined in (28) are also calculated according to the used Δf and are listed in Table 3 too.

Table 3
Mode cutoff frequencies (GHz) of slab-loaded rectangular waveguide (TM polarization)

M	N_x, N_y	$\Delta t, t$	Δf	h	f_c	RSK		FDTD	
						$\hat{f}_c$	e_f	$\hat{f}_c$	e_f
24	26, 51	2(−5), 2	0.15	117.9205	16.0218	16.0244	0	17.4862	10
				267.7900	19.7099	19.7094	0	19.2477	3
				326.6394	21.6386	21.6513	0	24.4587	19
				411.8359	24.7317	24.7401	0	26.8073	14
				512.1969	28.6893	28.6773	0	30.9174	15
32	51, 101	1(−5), 8	0.0375	117.9205	16.0218	16.0375	0	16.0000	1
				267.7900	19.7099	19.7125	0	19.6750	1
				326.6394	21.6386	21.6250	0	21.5875	1
				411.8359	24.7317	24.7375	0	24.6250	3
				512.1969	28.6893	28.6750	0	28.5250	4
				597.4794	32.2307	32.2000	1	32.0501	5
				649.0216	34.4280	34.4500	1	34.2251	5
				726.2445	37.7809	37.7875	0	37.3751	11
				816.4413	41.7686	41.6125	4	41.2751	13
				899.5953	45.4964	45.4750	1	44.8375	18
				953.2548	47.9226	47.4750	1	47.4251	13
				1020.940	51.0020	51.0251	1	50.0876	24

For $M = 24$ and 32, r is chosen as 2.9 and 4.2, respectively.

It can be seen from Table 3 that when a coarse mesh is used ($N_x = 26$, $N_y = 51$ and $\Delta t = 2 \times 10^{-5}$), the FDTD estimates have quite large errors which are around $10\Delta f$. However, the numerical results by using the DSCTD method with the RSK are in excellent agreement with analytical results. In terms of the error measurement (28), the DSCTD estimates are all exact. When a fine mesh is used ($N_x = 51$, $N_y = 101$ and $\Delta t = 10^{-5}$), the accuracy of the FDTD estimates improves greatly for the first five modes. Note that for these five modes, the DSCTD estimates are still exact. For high frequency modes, the FDTD estimates based on the fine mesh become unreliable quickly, whereas the DSCTD results are still in very good agreement with the analytical ones. When the frequency exceeds 50 GHz, the FDTD deviation is as large as $24\Delta f$, whereas the DSCTD one is only one Δf. Thus, the DSCTD is far more accurate than the FDTD for modeling the dielectric slab-loaded rectangular waveguide. The present numerical studies illustrate that the DSCTD algorithm is capable of providing highly accurate results when applying to the inhomogeneous media. It is worthwhile to pointed out that, however, the DSCTD estimates are no longer as accurate as the previous ones for the hollow rectangular waveguide, due to the inhomogeneous media.

3.3. Shielded microstrip line

The determination of mode cutoff frequencies based on the time-domain DSC technique is extended to a shielded microstrip line [18]. This problem is slightly more complicated than the previous two examples and it does not admit an exact solution. Fig. 7 shows the geometry of a single microstrip line within a square cross-sectional waveguide. The dielectric slab is located horizontally at the bottom portion of the waveguide. The relative permittivity and permeability of dielectric slab are $\epsilon_r = 8.875$ and $\mu_r = 1$, respectively. The lengths for the close square waveguide along the x- and y-coordinates are $a = b = 0.0127$ m and the dielectric-filled region is of height $d = 0.00127$ m. The waveguide is excited by injecting one-fourth of a Gaussian pulse, given by Eq. (26). For TM modes, axial z-components of the electric field are excited.

For the TM polarization, the interior region of the square cross-section is modeled by discretizing the region into many structured square cells and time increment is $\Delta t = 10^{-5}$. In computation, the thickness of the microstrip line is specified in terms of one single cell of the grid. For the DSCTD method, $M = 32$, $r = 4.2$ and $N_x = N_y = N = 61$ are chosen. The cutoff frequencies of TM mode estimated by the DSCTD for total calculated time $t = 6$ are shown in Table 4.

Since the analytical results are unavailable, an advanced commercial software, high frequency structure simulator (HFSS) [36], is employed to provide a reference solution. HFSS is based on the finite element method together with adaptive meshing [37]. For the present study, the mode cutoff frequencies can be approximated via a frequency domain eigenvalue problem by the HFSS [36,37]. Usually, the direct modeling in
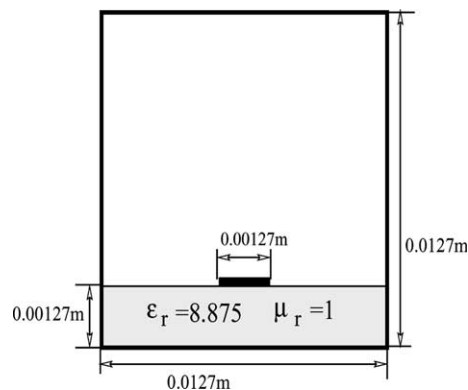

Fig. 7. Shielded microstrip line.

Table 4
The comparison of mode cutoff frequencies (GHz) between DSCTD and HFSS methods

$\hat{f}_c$ (DSCTD)	f_c (HFSS)	D_f
16.8303	16.8977	1
22.7529	22.7337	0
23.5825	23.5520	1
27.6987	27.6291	1
29.3272	29.3668	1

For DSCTD, $t = 6$, thus $\Delta f = 0.05$.

frequency domain attains much more accurate results than those of the time domain estimation, since there are extra factors which affect the final accuracy, such as the size of Δf and the selection of initial excitation, in the time domain estimation. For the present shielded microstrip line, the mode cutoff frequencies obtained by HFSS with a regular parameter setting [36] are also given in Table 4. By treating HFSS result as reference value f_c, we similarly define the difference between the DSCTD estimates $\hat{f}_c$ and f_c as

$$D_f = \left\lfloor \left| \frac{|f_c - \hat{f}_c|}{\Delta f} \right| \right\rfloor, \tag{34}$$

The differences are also given in Table 4. It is seen from Table 4 that the cutoff frequencies estimated by the DSCTD are almost the same as those of the HFSS. The difference between them is at most one Δf. Thus, the DSCTD modeling of shielded microstrip line is also very accurate.

3.4. Dielectric square

To further explore the potential of the DSCTD algorithm for electromagnetic simulations, we consider the wave scattering by a dielectric square in this section. The problem being considered is a generalization of that introduced by Jurgens and Zingg [38] with the same geometric structure. In particular, the domain under consideration is a unit square, $\Omega = [0, 1] \times [0, 1]$, where the dielectric material with permittivity $\epsilon = 4$ is located in the center of the domain, $0.4 \leqslant x \leqslant 0.6$, $0.4 \leqslant y \leqslant 0.6$, and is surrounded by the air ($\epsilon = 1$), see Fig. 8.

In the present study, we consider a high frequency Gaussian pulse incident upon the dielectric square at an angle of $\pi/4$. The incident electric field is given by

$$E_z(x, y, t) = \exp\left[-\frac{1}{2\gamma^2} \left(x\cos\frac{\pi}{4} + y\sin\frac{\pi}{4} + \frac{1}{2} - t \right)^2 \right] \cos\left[k\left(x\cos\frac{\pi}{4} + y\sin\frac{\pi}{4} + \frac{1}{2} - t \right) \right], \tag{35}$$

where k is the wavenumber and γ is the size of the Gaussian window. When $k = 0$, the incidence (35) is a normal Gaussian pulse which is the same as the one studied in [38]. When a larger k is used, the incident pulse consists of waves of higher frequency, see Fig. 9. A fixed $\gamma = 0.03$ was used in [38]. In this paper, we consider different γ values to generate different incident pulses. It is clear from Fig. 9 that when a larger γ is used, the pulse is widened and the number of multiple waves increases. By using nontrivial values of k and γ, the incident pulse (35) typically represents a high frequency wave which is commonly encountered in the real-world electromagnetic applications.

It is well known that the problem of short wave remains a great challenge to the low-order FD methods [39]. This is mainly due to the fact that the FD method suffers from relatively large dispersive error. For example, to achieve a reasonably good accuracy, a discretization about 18 grid points per minimal wavelength (PPW) is usually required by the FDTD method [39]. Thus, the FDTD is efficient only for geometries of moderate size. For multi-dimensional large-scale problems that are hundreds of wavelengths in size, the grid size required by using the FDTD method could become excessively expensive on modern
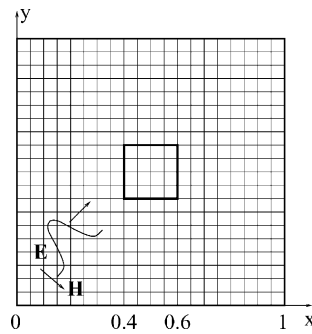
Fig. 8. An example grid and the geometry of the problem of dielectric square.
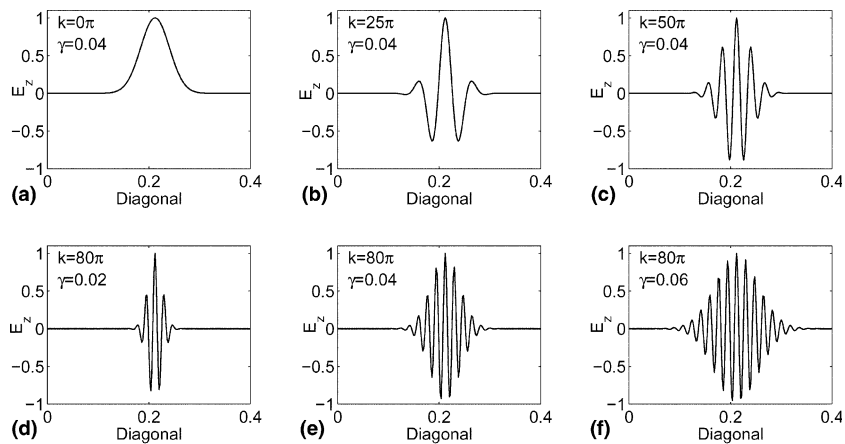

Fig. 9. Example plots of the incident pulse $E_z(x, y, t)$ along the diagonal. The pulse is considered to be propagated in the free space up to the time $t = 0.8$.

computers. This calls for the novel development of highly accurate numerical methods for electromagnetic and acoustic wave computations in the literature [39,40]. Therefore, it is of great interest in the present study to explore the potential use of the DSCTD method for the problem of short wave, and this is the reason for us to construct the high frequency pulse (35).

We first consider the problem of wave propagation of the pulse (35) in the free space up to the time $t = 0.8$. Note that from Fig. 9 the wave front of the pulse (35) still does not reach the dielectric square when $t = 0.8$. Considerable understandings can be gained in the study of wave propagations in the free space, which are useful to the study of wave scattering.

In the present study, the same boundary conditions as those in [38] are used. In particular, the incident field is imposed along the entire outer boundary, and spurious reflections at boundaries are not considered because the simulation is not run long enough for the reflected pulse to reach the boundaries. It is noted that a standard Fourier pseudospectral method cannot be utilized for the present problem, since the boundary condition is not periodic. For modeling evanescent electromagnetic waves, a pseudospectral time domain (PSTD) method [31] has been successfully developed. The PSTD scheme uses the perfectly matched layer (PML) [41] technique to bypass its limitation on periodic boundary conditions, so that it seems to be applicable to the present test problem. However, the utility of the PSTD method remains to be difficult because it is not clear whether it is possible to impose fields along the entire outer boundary while using the

PML. Furthermore, since the PML technique was specifically designed to absorb outgoing waves and there are no outgoing waves for the present simulation with short time, the use of the PML would be obviously unnecessary. In contrast, the DSCTD method can be easily implemented in this problem, owing to its flexibility in handling complex geometries and boundary conditions.

We consider a simple mesh in the present study. In [38], in order to attain an accurate simulation of a narrower pulse inside the dielectric square, the authors divided the computational domain into subdomains and imposed the grid density in the interior of the dielectric to be twice as that of the free space. On the interface between the dielectric and free spaces, a sophisticated interface treatment involving both the jump conditions and proper schemes of interpolation as well as extrapolation was employed to simulate the fields [38]. By controlling the error introduced by such a technical treatment, accurate solutions were reported [38]. In the present study, we could implement DSC algorithm in exactly the same manner as that of [38], since a DSC finite subdomain code is readily available [42]. In fact, a DSC based shock-capturing algorithm has been developed [43], which could also be used to handle the discontinuity in the dielectric media. However, to explore the ability of the DSC algorithm for electromagnetic wave computation, we intend to simply consider a uniform grid without resorting to sophisticated techniques. Here, a uniform grid of $\Delta = \Delta x = \Delta y$ is chosen for the entire computational domain.

To simulate the wave propagation, we choose the half bandwidth as $M = 32$ in the DSC algorithm, and the ratio r is optimally chosen by means of the Fourier dispersion analysis in each case and is reported. For a comparison, the second-order centered FD scheme (FD2) and fourth-order centered FD scheme (FD4) are also employed. The time marching scheme in both FD methods is also RK4. Moreover, a sufficiently small time increment $\Delta t = 1.0(-5)$ is employed in the studies of the free space so that the approximation error is mainly introduced by the spatial discretization. The numerical results of the free space simulation are summarized in Table 5. In this table, two sets of numerical experiments are considered. The

Table 5
Numerical errors in modeling the high frequency wave propagation in the free space

γ	k	Scheme	$\Delta = 0.01$			$\Delta = 0.005$			$\Delta = 0.0025$	
			r	L_∞	CPU	r	L_∞	CPU	L_∞	CPU
0.2	50π	FD2	—	7.57(−1)	85	—	2.01(−1)	501	5.10(−2)	2416
		FD4	—	1.05(−1)	109	—	6.98(−3)	711	4.51(−4)	2597
		DSC	4.1	6.63(−11)	436	3.7	7.12(−11)	1747		
0.2	100π	FD2	—	8.84(−1)	75	—	1.42(+0)	462	3.99(−1)	2420
		FD4	—	1.90(+0)	86	—	2.08(−1)	532	1.41(−2)	2654
		DSC	6.2	3.43(−7)	445	4.1	2.06(−10)	1740		
0.2	135π	FD2	—	1.77(+0)	74	—	1.84(+0)	447	9.48(−1)	2318
		FD4	—	2.19(+0)	85	—	8.38(−1)	505	6.18(−2)	2544
		DSC	20.2	3.81(−2)	436	4.5	2.68(−10)	1755		
0.1	60π	FD2	—	1.24(+0)	72	—	3.46(−1)	450	8.81(−2)	2563
		FD4	—	2.50(−1)	84	—	1.73(−2)	494	1.14(−3)	2735
		DSC	4.4	5.06(−11)	434	3.5	8.34(−11)	1746		
0.03	60π	FD2	—	1.14(+0)	73	—	3.54(−1)	588	9.28(−2)	2333
		FD4	—	2.98(−1)	86	—	2.17(−2)	636	1.42(−3)	2794
		DSC	5.6	7.40(−9)	503	3.5	1.20(−10)	1768		
0.01	60π	FD2	—	7.80(−1)	73	—	4.87(−1)	652	1.46(−1)	2539
		FD4	—	4.80(−1)	94	—	6.77(−1)	676	5.07(−2)	2593
		DSC	5.1	1.29(−2)	477	5.5	6.33(−9)	1771		

The computation is up to the time $t = 0.8$ with $\Delta t = 1.0(-5)$. For the DSC, $M = 32$, and an optimal r is used in each case and is reported.

wavenumber k is increased with a fixed Gaussian window size γ in one set, while in the other set, γ is decreased with a fixed k. The DSC algorithm is only calculated on two coarse meshes whereas two FD schemes are also considered on a fine mesh. Relative CPU time is reported.

In the present study, we will simply interpret result with its L_∞ error smaller than 0.05 to be sufficiently accurate. Note that the maximum value of the pulse is unit, so 5% is also the acceptable level of accuracy for engineering applications. We first consider the influence of changing k to the numerical accuracy, with a fixed $\gamma = 0.2$. To gain a quantitative insight, we consider a 1D Fourier spectrum analysis of the pulse E_z. In particular, we take a discrete Fourier transform of $E_z(x, 0, 0.8)$, i.e., the values of E_z along the x-axis at time $t = 0.8$, with respect to x. The corresponding Fourier responses with different k and Δ are depicted in Fig. 10. Note that E_z is translation invariant for different y values and there is a symmetry between x and y directions. Thus, the present 1D Fourier analysis is sufficient for revealing the spectral properties of E_z.

It can be observed from Fig. 10 that there exist two peaks in the spectrum of $E_z(x, 0, 0.8)$ within $[-\pi/\Delta, \pi/\Delta]$, the range of the Fourier frequency ω. The location of the peak values are determined by the wavenumber along x direction, i.e., $k_x = k\cos(\pi/4) = \sqrt{2}k/2$. However, unlike the spectrum of a single sinusoid, the peaks of the Fourier responses in Fig. 10 are not signal valued, but have wider supports. This is due to the Gaussian part in (35). It is well known that the Fourier response of a Gaussian is also a Gaussian in the spectral representation, while a production in the time domain is corresponding to a convolution in the Fourier domain. Therefore, after convolution with a Gaussian, the peaks attain the shape of a normal distribution. Because a fixed γ is used, all peaks in Fig. 10 have the same width. By using a quite large γ, the peaks of the spectrum are actually quite narrow. Thus, the characteristic of the spectrum is mainly determined by the center of the peaks, i.e., k_x. In the time domain, this means that the averaged wavelength in $E_z(x, 0, 0.8)$ along x (or y) direction will be near $\lambda_a = 2\pi/k_x$. Therefore, by using a mesh with size N, the averaged grid density in numerical computation will be around $\rho_a = 2\pi(N-1)/k_x = 2\sqrt{2}\pi(N-1)/k$ PPW.

For $k = 50\pi$ and $N = 101$ ($\Delta = 0.01$), the grid density is about $\rho_a = 5.66$ PPW in each dimension. This is a typical case of under sampling and it is difficult to achieve high computational accuracy. Since usually the FD2 scheme uses about 18 PPW [39], the FD2 errors are up to 0.75 as can be seen from Table 5. The FD4 results are also inaccurate in such an under sampling case. However, the DSC algorithm performs very well in such a challenging case, its L_∞ error is as small as $6.63(-11)$ and is about 10 orders more accurate than the FD schemes. When a doubled $N = 201$ is used, ρ_a is 11.31 PPW and the frequency of the pulse becomes relatively low with respect to the numerical resolution. Thus, it can be seen from Table 5 that by using a discretization with over 11 PPW, the FD4 accuracy is of satisfactory now. However, the FD2 accuracy
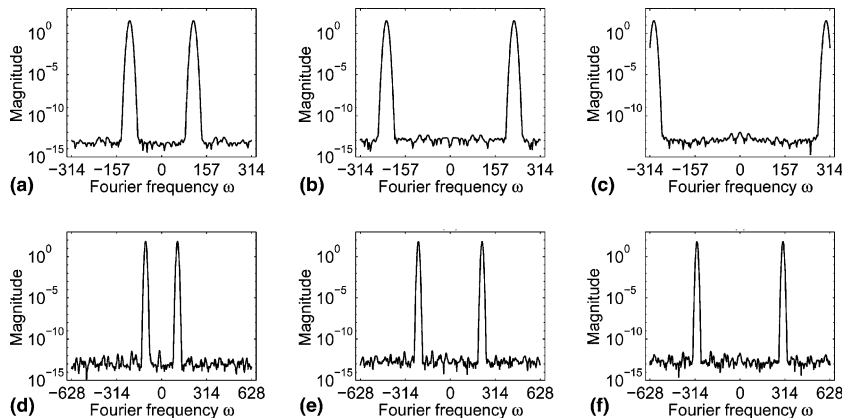

Fig. 10. Fourier spectrum analysis of $E_z(x, 0, 0.8)$. Here γ is fixed as 0.2. (a) $k = 50\pi$ and $\Delta = 0.01$; (b) $k = 100\pi$ and $\Delta = 0.01$; (c) $k = 135\pi$ and $\Delta = 0.01$; (d) $k = 50\pi$ and $\Delta = 0.005$; (e) $k = 100\pi$ and $\Delta = 0.005$; (f) $k = 135\pi$ and $\Delta = 0.005$.

reaches the acceptable level 5% only when $N = 401$, i.e., $\rho_a = 22.62$ PPW. It is noted that when N increases from 101 to 201, unlike those of two FD schemes, the accuracy of the DSC algorithm becomes slightly lower. This should be due to the limitation of finite precision or the error of temporal discretization. In other words, the DSC algorithm has already achieved the highest possible accuracy when $N = 101$. A larger mesh size N usually implies a longer computing time and a larger computer memory requirement. For the present study, it is clear from Table 5 that to achieve the acceptable level of accuracy, 5%, the required CPU time of the FD2 and FD4 is about 5 and 1.5 times of that of the DSC, respectively. This suggests that the DSC algorithm is cost-efficient comparing with the FD schemes for short wave problems.

When a larger $k = 100\pi$ is used, the numerical modeling is more challenging. For $N = 101$, the averaged grid density is as low as $\rho_a = 2.83$ PPW. Obviously, under such a case, it is extremely difficult for any numerical method to accurately catch up with the fast oscillations in the pulse. Amazingly, the DSC results are still accurate to 6 significant figures with $\rho_a = 2.83$ PPW. Moreover, when Δ is halved, the DSC results become over one thousand times more accurate. On the other hand, the FD2 results are all of huge errors for all tested mesh sizes. For the FD4 method, its accuracy is only acceptable when $N = 401$. So the FD4 approach requires about six times more CPU time than that of the DSC to deliver an acceptable accuracy when $k = 100\pi$.

When k is further pushed to be 135π, the averaged grid density is $\rho_a = 2.095$ PPW when $N = 101$. With such a low ρ_a, it is almost impossible to accurately model the highly oscillated multiple waves by any means. Furthermore, it is noted that in Chart (c) of Fig. 10, the peaks reach the boundaries, $\pm\pi/\Delta$. The quantity π/Δ is known as the Nyquist frequency, which is the maximum wavenumber that could be distinguished by the discretization with the mesh size Δ. Any wavenumber whose absolute value is great than the Nyquist frequency will be misinterpreted and contribute to the aliasing error. Consequently, the approximation error of any numerical approach is doomed to be very large. Even an "exact" approximation approach which is free of the dispersive and dissipative errors will yield large error. As shown in Fig. 10 the aliasing error is about 0.02 for this case. Due to these two factors, it can be seen from Table 5 that the L_∞ error of the DSC algorithm is 0.038 for this tough case. However, note that this accuracy is still of satisfactory for engineering applications, while the results of the FD2 scheme are too poor to be useful. Similar to the FD2 scheme, the FD4, is also unable to produce 5% accurate results even when $N = 401$ ($\rho_a = 8.38$ PPW), although it costs about 5.8 times more CPU than the DSC in this case. It should be addressed that when N is doubled from 101 to 201, the DSC L_∞ error is decreased over 8 orders of magnitude. This typically verified the spectral accuracy of the DSC algorithm [35].

In the second set of numerical experiments in Table 5, γ is decreased with a fixed $k = 60\pi$. In order to analyze these numerical results, a 1D discrete Fourier transform of $E_z(x, 0, 0.8)$ is similarly carried out for different γ and Δ, see Fig. 11. Likewise, there exist two peaks in each case. The peaks locate at the same position in each case, since k is fixed. Numerically, this suggests that the averaged grid density ρ_0 is fixed. The major affecting factor now is the width of peaks. It is obviously from Fig. 11 that the peaks broaden when γ is decreased. This is simply because a decrease of the Gaussian window size in the time domain will lead to an increase of the Gaussian bandwidth in the spectral domain. When $\gamma = 0.03$, two peaks are broadened enough to be merged at their intersection. When $\gamma = 0.01$, the aliasing error of $N = 101$ is obviously huge and is occurred even when $N = 201$. Therefore, one can conclude that for a fixed k, the smaller the γ is, the higher the frequency response of the pulse is.

The Fourier analysis considered in Fig. 11 reveals that the effect of decreasing γ is similar to that of increasing k. Numerical experiments in Table 5 also confirms this observation. In particular, the findings attained from the cases of $\gamma = 0.1$ and $\gamma = 0.03$ will be quite similar to those of the aforementioned cases of $k = 50\pi$ and $k = 100\pi$, respectively. When $\gamma = 0.01$, the aliasing error is very significant (about 0.02), which is also similar to $k = 135\pi$. For such an extremely challenging case, the DSC algorithm still yield accurate approximation when $N = 101$, while the spectral convergence [35] is observed again when $N = 201$. Similarly, the results of two FD schemes are of enormous error.
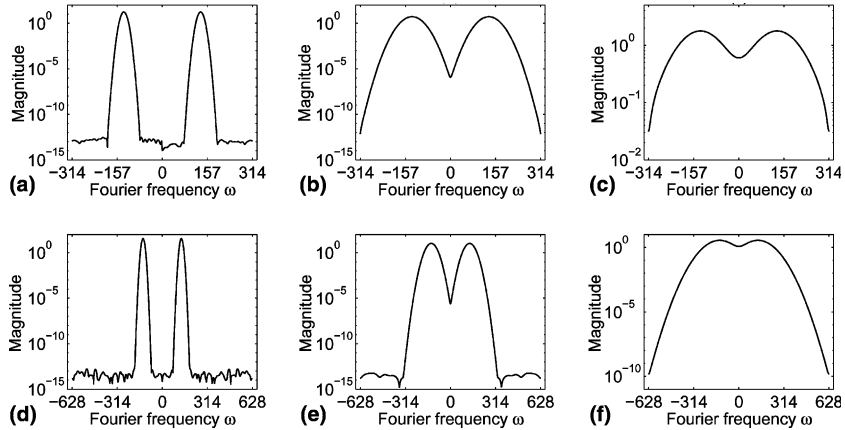
Fig. 11. Fourier spectrum analysis of $E_z(x, 0, 0.8)$. Here k is fixed as 60π. (a) $\gamma = 0.1$ and $\Delta = 0.01$; (b) $\gamma = 0.03$ and $\Delta = 0.01$; (c) $\gamma = 0.01$ and $\Delta = 0.01$; (d) $\gamma = 0.1$ and $\Delta = 0.005$; (e) $\gamma = 0.03$ and $\Delta = 0.005$; (f) $\gamma = 0.01$ and $\Delta = 0.005$.

The only difference between decreasing γ and increasing k is its influence to the averaged grid density ρ_a. When k is larger, ρ_a will be smaller, while the changing of γ does not alter ρ_a. Thus, numerical approximations of $\gamma = 0.01$ are relatively easier than those of $k = 135\pi$, especially when N is large. Therefore, the FD4 can give an accurate result when $\Delta = 0.0025$ for $\gamma = 0.01$. Note that now the CPU time of the FD4 is about 5.4 times of that of the DSC. On the other hand, by comparing among the L_∞ errors of the DSC algorithm with $N = 201$ of all cases, it can be found that the error of $\gamma = 0.01$ is the largest one. This is owing to the aliasing error, see Chart (f) of Fig. 11. In fact, this L_∞ error is of the same level of magnitude as the aliasing error. The same finding also holds for this case with $N = 101$. This demonstrates the robustness of the DSC algorithm for electromagnetic wave computation.

The numerical studies in the free space wave propagation indicate that the accuracy of a numerical scheme can be significantly reduced when the studied waves are of high frequency or of large aliasing error. We will next consider the problem of wave scattering from the dielectric square by using the incidence (35) with $\gamma = 0.04$ and $k = 25\pi$. This is a very challenging study, since both problems of short wave and inhomogeneous media are presented. It is known that for the electromagnetic problems with discontinuous media, the full accuracy of the numerical method may not be realized [38,44]. To attain a high accurate simulation, special attention is to be paid. In the present study, to account for the discontinuity in the electric flux density, a simple ϵ-smoothing technique [44] which replaces the discontinuous permittivity function ϵ by a fourth-order accurate smooth implicit approximation is utilized. In two dimensions, the fourth-order interpolation is achieved by using [44]

$$\left(I + \frac{\Delta^2}{8}\nabla^2\right)\epsilon_{i,j} = \frac{\epsilon_{i+1/2,j+1/2} + \epsilon_{i-1/2,j+1/2} + \epsilon_{i+1/2,j-1/2} + \epsilon_{i-1/2,j-1/2}}{4}, \tag{36}$$

where ∇^2 is the standard approximation to the Laplacian and I is the identity matrix.

In the DSC algorithm, the half bandwidth is chosen as $M = 8$ with $r = 2.4$. The RK4 with a small $\Delta t = 0.0005$ is used in all three methods: the FD2, the FD4 and the DSC, for the study of wave scattering. The ϵ-smoothing technique [44] is used in all computations. A reference solution of the electric field intensity at $t = 1.4$ which is generated by using very fine mesh ($\Delta = 0.0025$) is given in Chart (a) of Fig. 12. Multiple waves are clearly presented in the pulse and fast oscillations occur inside the dielectric square. In comparing with this reference solution, the approximation errors in the electric field resulted from three schemes are depicted in Fig. 12. Here, the mesh size of the FD4 and DSC is the same ($\Delta = 0.01$), while a
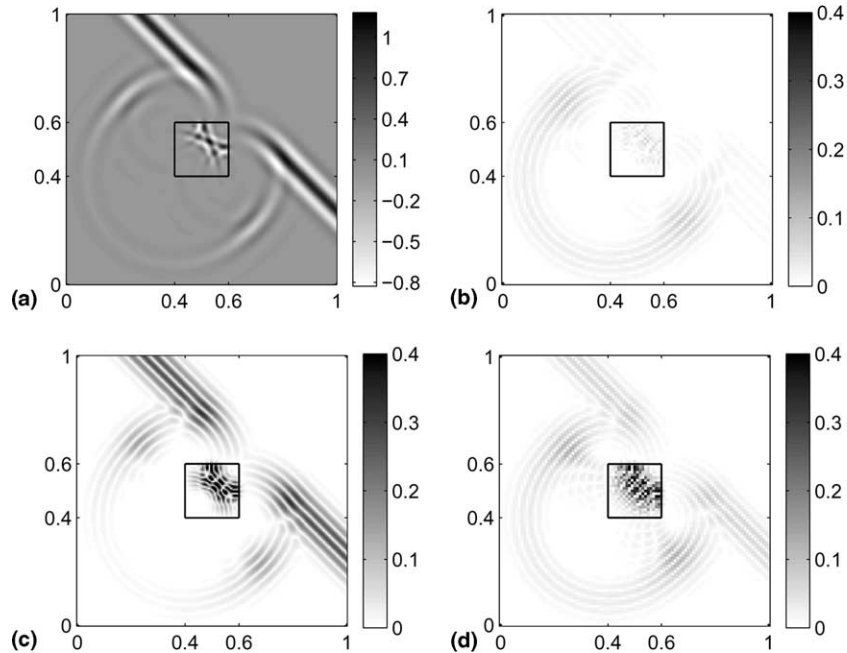
Fig. 12. Contour plots of electric field and errors in electric field. (a) The reference solution generated by using the DSC algorithm with $\Delta = 0.0025$; (b) DSC error ($\Delta = 0.01$); (c) FD2 error ($\Delta = 0.005$); (d) FD4 error ($\Delta = 0.01$).

smaller $\Delta = 0.005$ is used in the low accuracy scheme, the FD2. It is seen from Fig. 12 that the FD2 and FD4 yield extremely large approximation errors, their L_∞ errors are actually larger than 0.6, while the DSC accuracy is good enough for engineering applications.

To obtain comparable results as the DSC, a finer mesh has to be employed for both the FD2 and FD4, see Figs. 13 and 14. Since the major approximation errors and variations of the electric field occur inside the dielectric square, we focus only on this part in both figures. The enlarged plots given in Charts (c) and (d) of Fig. 13 clearly illustrate how large the errors are in the approximations of the FD2 with $\Delta = 0.005$ and the FD4 with $\Delta = 0.01$, see also Chart (b) of Fig. 14. A very large phase-lag can be clearly observed from Chart (a) of Fig. 14. Note that, at the same time, strong oscillation is generated at the tail of the pulse in the numerical solution obtained by using the FD4 with $\Delta = 0.01$. Both phenomena are typical outcomes of numerical dispersion. The approximation is improved when a finer mesh is used. By using $\Delta = 0.0025$, the errors of the FD2 are greatly reduced, see Chart (e) of Fig. 13. However, they are still much larger than those of the DSC with $\Delta = 0.01$, although the FD2 requires about 11.4 times as much CPU time as the DSC. The L_∞ error of the FD2 could be as large as 0.2, see Chart (b) of Fig. 14. By using $\Delta = 0.005$, the FD4 accuracy greatly improves to be satisfactory (Chart (f) of Fig. 13), which is comparable to that of the DSC, as can be seen from Chart (d) of Fig. 14. However, now the CPU time of the FD4 is about 2.6 times of that of the DSC. The present studies clearly indicate that the DSC algorithm significantly outperforms both the FD2 and FD4. It is noted in Chart (c) of Fig. 14 that there are some differences between the DSC curve and the reference solution. In particular, it misses two peaks of negative values. This is because the used mesh is too coarse in the DSC so that there is no sampling points at those valley floors. It is, therefore, striking that the DSC algorithm is still capable of producing high accurate results on such a coarse grid. It is also noted that, due to its high accuracy, the ϵ-smoothed DSC algorithm is employed with $\Delta = 0.0025$ to generate the reference solution of this example.
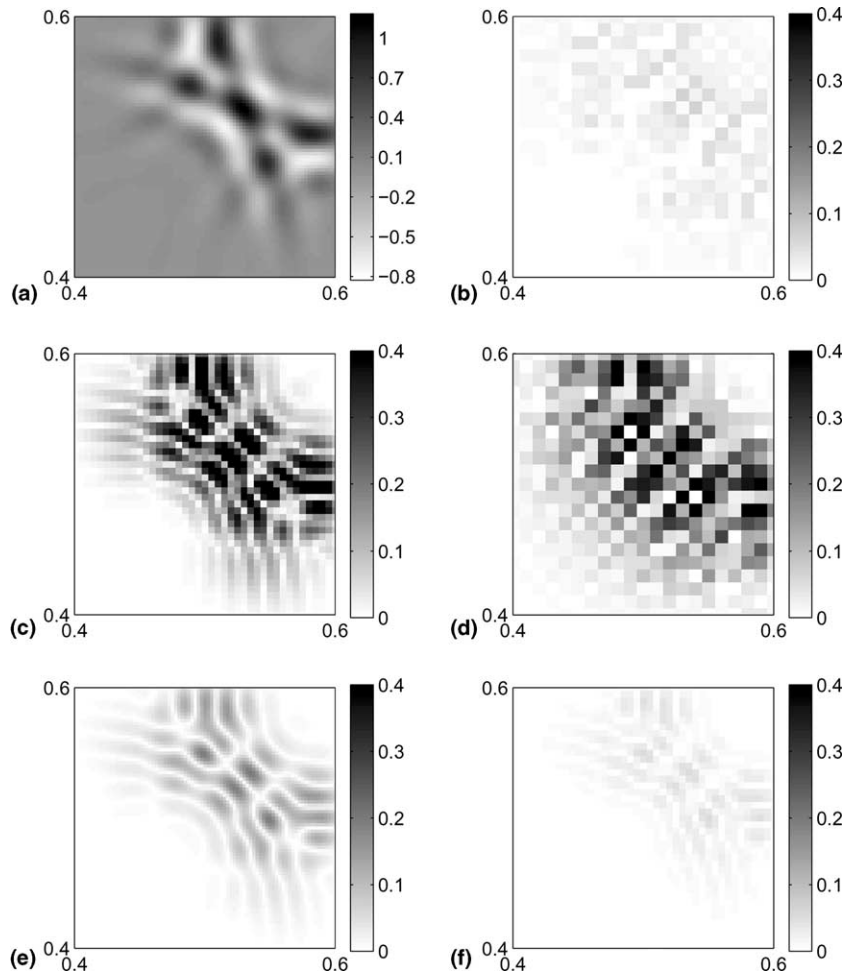
Fig. 13. Contour plots of electric field and errors in electric field inside the dielectric square. (a) The reference solution generated by using the DSC algorithm with $\Delta = 0.0025$; (b) DSC error ($\Delta = 0.01$); (c) FD2 error ($\Delta = 0.005$); (d) FD4 error ($\Delta = 0.01$); (e) FD2 error ($\Delta = 0.0025$); (f) FD4 error ($\Delta = 0.005$).

To further analyze the numerical results, a Fourier spectrum analysis of numerical solutions is conducted. Due to the symmetry between x and y directions, we only consider the Fourier analysis of $E_z(x, y_i, 1.4)$, with different $y_j = (j - 1)\Delta$ for $j = 1, \ldots, N$. The Fourier spectrum analyses of the DSC results with $N = 101$ and $N = 201$ are given in Figs. 15 and 16, respectively. It is clear from Fig. 15(a) that the electric field after scattering has more high frequency components besides the peaks at k_x. These high frequency components form some sub-peaks with wide supports. The generation of higher frequency components in E_z is because that the wave speed inside the dielectric is one half the value outside the dielectric. As a consequence, the waves of the pulse are compressed inside the dielectric. This can be seen more clearly from Fig. 16, where the Fourier spectrums for different y ranges are plotted in different charts. For the middle one which corresponds to y_i on the dielectric, the sub-peaks are obviously presented. When y_i is not on the dielectric, there are only a few sub-peaks which are of very small magnitude. These sub-peaks correspond to $E_z(x, y_i, 1.4)$ with y_i close to the dielectric and are artificially created in the numerical
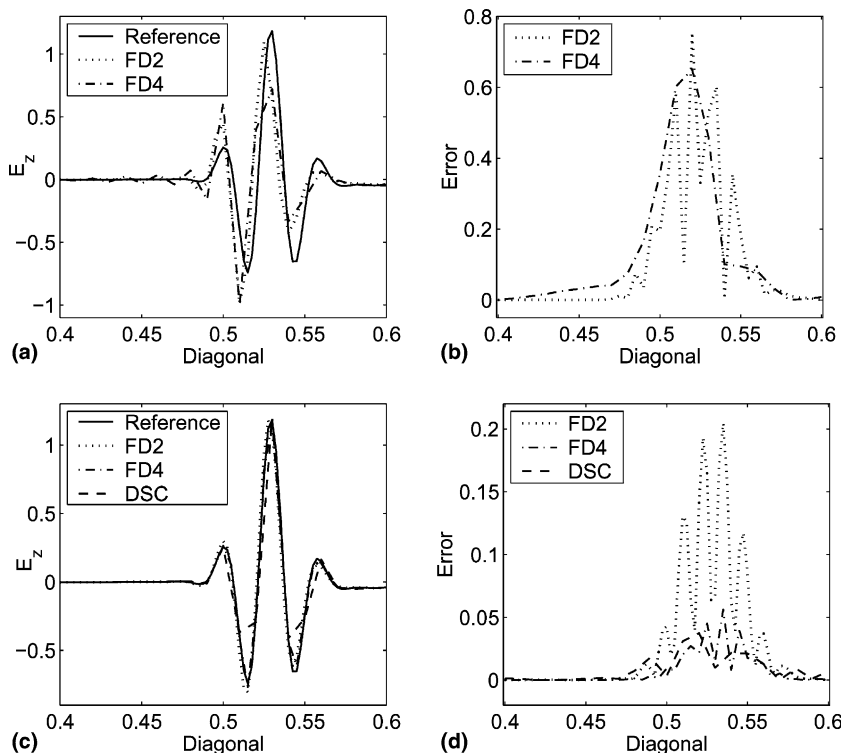
Fig. 14. Electric field across diagonal of dielectric square. (a) Electric fields approximated by the FD2 with $\varDelta = 0.005$ and the FD4 with $\varDelta = 0.01$; (b) absolute errors of the electric fields in (a); (c) electric fields approximated by the FD2 with $\varDelta = 0.0025$, the FD4 with $\varDelta = 0.005$, and the DSC with $\varDelta = 0.01$; (d) absolute errors of the electric fields in (c).
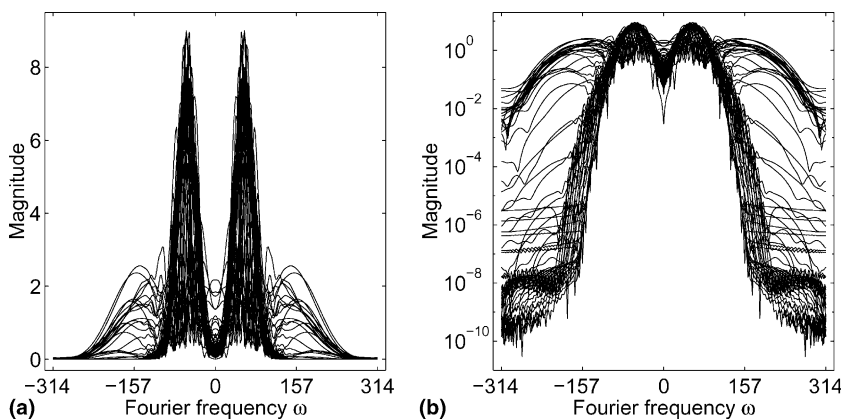

Fig. 15. Fourier spectrum analysis of $E_z(x, y_i, 1.4)$ with $N = 101$. (a) Fourier spectrum; (b) Fourier spectrum in the log scale.

computations. When y_i is far away from the dielectric, the spectrums clearly contains only two peaks around $\pm k_x$ in Chart (a) and (c) of Fig. 16.

The second observation from two figures is that sub-peaks also decay due to the effect of the Gaussian in (35). However, by using $(\gamma, k) = (0.04, 25\pi)$, the aliasing error when $N = 101$ is as large as about 0.07.
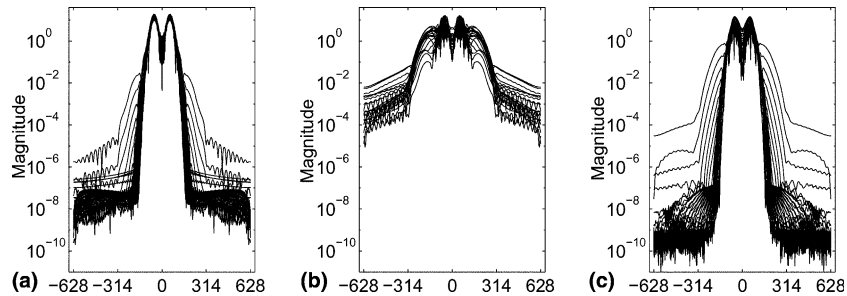
Fig. 16. Fourier spectrum analysis of $E_z(x, y_i, 1.4)$ with $N = 201$. (a) Fourier spectrum of $E_z(x, y_i, 1.4)$ with $0 \leqslant y_i < 0.4$; (b) Fourier spectrum of $E_z(x, y_i, 1.4)$ with $0.4 \leqslant y_i \leqslant 0.6$; (b) Fourier spectrum of $E_z(x, y_i, 1.4)$ with $0.6 < y_i \leqslant 1$.

Therefore, the present problem with $(\gamma, k) = (0.04, 25\pi)$ is extremely difficult to solve numerically. Both FD methods fail to provide accurate simulation when the mesh is coarse. Nevertheless, the DSC results are still of 5% accuracy under such a difficult situation.

When $N = 201$, we find that the spectrum inside the dielectric has two transition points, at which the exponential decays of sub-peaks become a polynomial one. The transition points locate around $\omega = \pm 100\pi$. The Fourier spectrum analysis of $N = 401$ has been carried out although not showing here, since almost identical pattern was found. In particular, the frequency components on $\omega \in [200\pi, 400\pi]$ of $N = 401$ were found to decay at the same slope as those on $\omega \in [100\pi, 200\pi]$ of $N = 201$. For the present Fourier spectrum analysis with $N = 201$, the slow decaying parts at high frequency band $\omega \in [100\pi, 200\pi]$ are believed to be linked to the discontinuous nature of the media. The discontinuity in the media coefficients introduces additional approximation errors in numerical computation, which will be referred to as discontinuous errors here. The discontinuous errors occur at interfaces of materials, thus the high frequency components with slow decaying appear only in the middle chart of Fig. 16. Furthermore, the decaying rate of these high frequency components with respective to Δ is of second order, which is the same as that of the discontinuous error [44]. From the present Fourier analysis, one can conclude that the frequency response of the discontinuous error involves all frequencies with a second-order decaying rate. Therefore, the discontinuous error will limit all kinds of approximations to be second-order accurate, no matter what kind of numerical discretization is performed. For the present modeling based on a uniform mesh, the substantial improvement in accuracy can only be achieved by increasing the mesh resolution. However, it is noted that the present test problem with $(\gamma, k) = (0.04, 25\pi)$ was especially chosen such that the transition points of spectrums locates at the Nyquist frequency with $N = 101$. Consequently, when $N = 101$, the errors introduced by the high frequency wave simulation (i.e., sub-peaks) dominant the discontinuous errors. Therefore, similar to the studies of free space, for this short wave problem, the DSC algorithm significantly outperforms the FD4 scheme.

4. Conclusions

In this paper, the discrete singular convolution time domain (DSCTD) algorithm is introduced to solve Maxwell's equations. The dispersion analysis of the DSC algorithm by means of the discrete Fourier transform is briefly discussed. Several numerical experiments are carried out to illustrate the high accuracy of the DSC algorithm for practical electromagnetic applications. The use of the DSC algorithm for electromagnetic problems with inhomogeneous media and nonstandard boundary conditions is explored.

The ability of the DSC algorithm for electromagnetic applications is extensively explored in the time domain wave computations of the hollow rectangular waveguide. The accuracy of the DSC algorithm is

illustrated to be much higher than those of the FDTD method and the scaling function multi-resolution time domain (S-MRTD) method with a Battle–Lemarie wavelet scaling function. Moreover, the DSC algorithm can achieve the spectral accuracy of global methods [35]. Hence, the machine precision can be reached by using a still quite coarse mesh. The property of the DSC algorithm on providing controllable accuracy is numerically verified. The present DSCTD algorithm is demonstrated to be cost-efficient.

The numerical prediction of mode cutoff frequency is also studied by using the DSCTD for three different waveguides, hollow rectangular waveguide, dielectric slab-loaded rectangular waveguide, and shielded microstrip line. The mode cutoff frequencies are obtained via a Fourier transform of the simulated time domain signals. Hence, the accuracy in estimates of cutoff frequencies is limited by the spectral spacing Δf. For the hollow rectangular waveguide, the DSC estimates are almost exact in terms of Δf, up to 150 GHz, which is much more accurate than those of the FDTD. The same finding is observed when the studied media is inhomogeneous in the dielectric slab-loaded rectangular waveguide. However, the accuracy of the DSCTD estimates is slightly reduced due to the influence of the discontinuous permittivity function in this case. For a more complicated waveguide, the shielded microstrip line which does not admit an exact solution, the DSC estimates are found be in very good agreement with results obtained by a popular finite element software.

The use of the DSC algorithm for electromagnetic wave computation is further considered in the scattering problem of a dielectric square. The considered pulse is of high frequency. By means of Fourier spectrum analysis, the propagation of the high frequency Gaussian pulse in the free space is thoroughly studied. The DSC algorithm can still yield accurate simulations when the averaged grid density is only 2.095 grid points per wavelength (PPW) and/or when the aliasing error is as large as 0.02. However, to achieve an acceptable accuracy, a discretization over 18 PPW and 9 PPW is usually required for the FD2 and FD4 schemes, respectively. For these short wave problems, the savings in the computational effort are noticeable by using the DSC algorithm. In the study of high frequency wave scattering, the test problem is especially chosen such that the errors introduced by modeling high frequency wave dominant the errors induced by the discontinuous permittivity function. Meanwhile, to account for the discontinuity in the electric flux density, the discontinuous permittivity function is treated by using a simple ϵ-smoothing technique [44]. For this extremely challenging problem, the DSC can still provide very accurate approximations, while two FD schemes suffers from strong numerical dispersion. To the best of our knowledge, the DSC algorithm is the only available method which can deliver high accuracy for this tough problem, so far.

In the present study, we have also tested the ability of the DSC algorithm in handling complex geometries and boundary conditions. In this regard, we have used the DSC algorithm for two closed waveguides with inhomogeneous media. The problem of short-time open-space wave scattering has also been successfully treated in the DSC algorithm, which remains a challenge to global methods. Since the DSCTD algorithm is a local method in general, it has similar flexibility as the FDTD in handling homogeneous and inhomogeneous microwave problems. Because the DSC algorithm can deal with some complex boundary conditions which are difficult to global methods, it can be served as a suitable alternative to the pseudo-spectral time domain (PSTD) method to deliver high accuracy for electromagnetic wave computations. In summary, the present studies indicate that the DSC algorithm is accurate, flexible and efficient for time domain electromagnetic wave computations.

Based on the present study, several remarks can be made about the developments of a more versatile numerical scheme in the framework of the DSC algorithm for computational electromagnetics. In the present study, the time stepping scheme used in the DSCTD is the fourth-order Runge–Kutta (RK4) scheme. It should be noted that, however, any other standard temporal discretization scheme can be used in associated with the DSC algorithm. One disadvantage of the RK4 scheme is its need to save temporary data, so that the DSCTD method requires more memory than the FDTD. In viewing of this, symplectic integrator propagator (SIP) time domain scheme may be a good alternative. Because SIP does not require to save temporary data, SIP scheme combined with RSK may need less memory than standard FDTD

method. Furthermore, since SIP is usually more stable than Runge–Kutta scheme, a larger time increment is permitted so as to save more computation time. Further research on this issue is under consideration.

In the present study, the loss of accuracy when the media is inhomogeneous is studied by means of the Fourier spectrum analysis. It is found that such a loss is mainly due to the discontinuity error, which generates infinitely high frequency response. An ϵ-smoothing technique [44] is employed in the present study to improve the convergence of higher-order numerical methods. However, since the ϵ-smoothing technique is still of low order, the accuracy of the DSC algorithm is degraded. In fact, when the DSC algorithm is tuned to higher accuracy by using larger M values, their results are all identical to the reported one. This is quite different from the previous numerical results in the hollow rectangular waveguide. Therefore, one can conclude that for the present example, the performance of the DSC algorithm is limited by the discontinuity error. The DSC algorithm is expected to perform better when a much higher-order smoothing technique or other sophisticated interface treatment is used [12]. Alternatively, a DSC finite subdomain method [42] may be used to improve the mesh resolution. The utility of more advanced techniques to account for the inhomogeneous media in the DSC algorithm is currently in progress.

References

[1] K.S. Yee, Numerical solution of initial boundary value problems involving Maxwell's equations in isotropic media, IEEE Trans. Antennas Propagat. 14 (1976) 302–307.
[2] T.A. Driscoll, B. Fornberg, Note on nonsymmetric finite differences for Maxwell's equations, J. Comput. Phys. 161 (2000) 723–727.
[3] A.H. Mohammadian, V. Shankar, W.F. Hall, Computation of electromagnetic scattering and radiation using a time-domain finite-volume discretization procedure, Comput. Phys. Commun. 68 (1991) 181–262.
[4] J.S. Hesthaven, T. Warburton, Nodal high-order methods on unstructured grids – I. Time-domain solution of Maxwell's equations, J. Comput. Phys. 181 (2002) 186–221.
[5] Z. Baharav, Y. Leviatan, Wavelets in electromagnetics: the impedance matrix compression (IMC) method, Int. J. Numer. Model. El. 11 (1998) 69–84.
[6] M. Krumpholz, L.P.B. Katehi, MRTD: new time-domain schemes based on multiresolution analysis, IEEE Trans. Microwave Theory Tech. 44 (1996) 555–571.
[7] E.M. Tentzeris, R.L. Robertson, J.F. Harvey, L.P.B. Katehi, Stability and dispersion analysis of Battle–Lemarie-based MRTD schemes, IEEE Trans. Microwave Theory Tech. 47 (1999) 1004–1013.
[8] M. Fujii, W.J.R. Hoefer, Time-domain wavelet Galerkin modeling of two-dimensional electrically large dielectric waveguides, IEEE Trans. Microwave Theory Tech. 49 (2001) 886–892.
[9] J.R. Treurniet, N.R.S. Simons, G.E. Bridges, Integer lattice gas automata for computational electromagnetics, IEEE Trans. Microwave Theory 48 (6) (2000) 985–990.
[10] L.S. Andersen, J.L. Volakis, Development and application of a novel class of hierarchical tangential vector finite elements for electromagnetics, IEEE Trans. Antenn. Propag. 47 (1999) 112–120.
[11] L.E. Garcia-Castillo, M. Salazar-Palma, Second-order Nedelec tetrahedral element for computational electromagnetics, Int. J. Numer. Model. El. 13 (2000) 261–287.
[12] T.A. Driscoll, B. Fornberg, A block pseudospectral method for Maxwell's equations – I. One-dimensional case, J. Comput. Phys. 140 (1998) 47–65.
[13] J.M. Song, C.C. Lu, W.C. Chew, S.W. Lee, Fast Illinois Solver Code (FISC), IEEE Trans. Antenn. Propag. 40 (1998) 27–34.
[14] T. Honma, Advanced Computational Electromagnetics, IOS Press, Ohmsha, 1995.
[15] H. Tsuboi, I. Sebestyen, Applied Electromagnetics and Computational Technology, IOS Press, Amsterdam, 1997.
[16] A.F. Peterson, S.L. Ray, R. Mittra, Computational Method for Electromagnetics, Oxford University Press, Oxford, 1998.
[17] K. Umashankar, A. Taflove, Computational Electromagnetics, Artech House, Boston, 1993.
[18] S.M. Rao, Time Domain Electromagnetics, Academic Press, San Diego, 1999 (Chapter 6).

[19] Y.Y. Lu, One-way large range step methods for Helmholtz waveguides, J. Comput. Phys. 152 (1999) 231–250.

[20] G.W. Wei, Discrete singular convolution for the solution of the Fokker–Planck equations, J. Chem. Phys. 110 (1999) 8930–8942.

[21] G.W. Wei, A unified approach for solving the Fokker–Planck equation, J. Phys. A 33 (2000) 343–352.

[22] G.W. Wei, Wavelets generated by using discrete singular convolution kernels, J. Phys. A 33 (2000) 8577–8596.

[23] G.W. Wei, Y.B. Zhao, Y. Xiang, Discrete singular convolution and its application to the analysis of plates with internal supports. I. Theory and algorithm, Int. J. Numer. Methods Engrg. 55 (2002) 913–946.

[24] G.W. Wei, A new algorithm for solving some mechanical problems, Comput. Methods Appl. Mech. Engrg. 190 (2001) 2017–2030.

[25] D.C. Wan, B.S.V. Patnaik, G.W. Wei, Discrete singular convolution-finite subdomain method for the solution of incompressible viscous flows, J. Comput. Phys. 180 (2002) 229–255.

[26] G.W. Wei, Vibration analysis by discrete singular convolution, J. Sound Vibr. 244 (2001) 535–553.

[27] Y.B. Zhao, G.W. Wei, Y. Xiang, Plate vibration under irregular internal supports, Int. J. Solids Struct. 39 (2002) 1361–1383.

[28] G.W. Wei, A unified method for solving Maxwell's equation, in: Proceedings of 1999 Asia-Pacific Microwave Conference, Singapore, 1999, pp. 562–565.

[29] B. Fornberg, A Practical Guide to Pseudospectral Methods, Cambridge University Press, Cambridge, 1996.

[30] S.Y. Yang, Y.C. Zhou, G.W. Wei, Comparison of the discrete singular convolution and Fourier pseudospectral methods for solving partial differential equations, Comput. Phys. Commun. 143 (2002) 113–135.

[31] Q.H. Liu, The PSTD algorithm: a time-domain method requiring only two cells per wavelength, Microwave Opt. Techn. Lett. 15 (1997) 158–165.

[32] G.W. Wei, D.S. Zhang, D.J. Kouri, D.K. Hoffman, Lagrange distributed approximating functionals, Phys. Rev. Lett. 79 (1997) 775–779.

[33] D. Gottlieb, C.W. Shu, On the Gibbs phenomenon and its resolution, SIAM Rev. 39 (1997) 644–668.

[34] R. Vichnevetsky, J.B. Bowles, Fourier Analysis of Numerical Approximations of Hyperbolic Equations, SIAM, Philadelphia, 1982.

[35] G. Bao, G.W. Wei, and S. Zhao, Numerical solution of the Helmholtz equation with high wavenumbers, Int. J. Numer. Methods Engrg., 2003 (in press).

[36] Ansoft Corporation, Getting started: an eigenmode problem, Available from http://www.ansoft.com/,2001.

[37] F.A. Fernandez, Y.L. Lu, Microwave and Optical Waveguide Analysis by the Finite Element Method, Research Studies Press, Hertfordshire, UK, 1996.

[38] H.M. Jurgens, D.W. Zingg, Numerical solution of the time-domain Maxwell equations using high-accuracy finite-difference methods, SIAM J. Sci. Comput. 22 (2000) 1675–1696.

[39] D.W. Zingg, Comparison of high-accuracy finite difference methods for linear wave propagation, SIAM J. Sci. Comput. 22 (2000) 476–502.

[40] O.C. Zienkiewicz, Achievements and some unsolved problems of the finite element method, Int. J. Numer. Methods Engrg. 47 (2000) 9–28.

[41] J.P. Berenger, A perfectly matched layer for the absorption of electromagnetic waves, J. Comput. Phys. 114 (1994) 185–200.

[42] D.C. Wan, B.S.V. Patnaik, G.W. Wei, Discrete singular convolution-finite subdomain method for the solution of incompressible viscous flows, J. Comput. Phys. 180 (2002) 229–255.

[43] G.W. Wei, Y. Gu, Conjugated filter approach for solving Burgers' equation, J. Comput. Appl. Math. 149 (2002) 439–456.

[44] E. Turkel, High-order methods, in: A. Taflove (Ed.), Advances in Computational Electrodynamics: The Finite-Difference Time-Domain Method, Artech House, Boston, MA, 1998 (Chapter 2).